Possible use of rotational ground motions in oilfield studies:

Part II: Synthetic seismograms and processing results

N.D. Pham, H. Igel, M. Käser
Department of Earth Sciences, LMU Munich

Last changes: May 21, 2009

This is a report under a *Confidential Information Disclosure Agreement* between the Ludwig-Maximilians-University, Munich, and Schlumberger K.K., Japan.

Table of Contents

Abstract

In this study we investigate in detail the possible use of joint measurements of rotational and translational motions in oilfield applications using synthetic data. First, we implement numerical simulations to output six-component synthetic seismograms of both rotational and translational motions. Then, we process the simulated data focusing on aspects that might be relevant for reservoir problems. We show that with joint measurements of translational and rotational motions one can: 1) separate S from P waves; 2) estimate the propagation direction of S waves by using polarizations of the two motion types (i.e. translation and rotation); 3) determine S-wave slowness from a linear array of borehole receivers.

1. Introduction

Recently, with the advances of observation instruments the earthquake induced rotational ground motions can be measured consistently (McLeod et al., 1998; Pancha et al., 2000, Schreiber et al., 2006, 2009, Wassermann et al., 2009). As a consequence, studies based on joint measurements of both translational and rotational ground motions grow rapidly (Igel et al., 2005, 2007, Cochard et al., 2006, Suryanto, 2006; Pham et al., 2009a, 2009b; Ferreira and Igel, 2009; Fichtner and Igel, 2009, Bernauer et al., 2009). The results of those studies show high potential of rotational signals in all aspects of seismological investigations (see Part I of this report).

In this report we focus on processing options when records of both translational and rotational motions are available. Here six-component seismograms are synthetically simulated. The structure of the report is as follows: In **Section 2** we present the simulation method and model setup to output six component seismograms. The processing results obtained from the simulated data are reported in **Section 3**. In this section, for purpose of separation of S and P waves, we examine the similarity of the waveforms of rotation rates and translational accelerations as well as the sensitivity of energy of rotational signals with the appearance of S waves. For the estimation of wave propagation directions we show a method using the polarizations of translational and rotational motions of S waves. The determination of S wave slowness based on joint measurements of translational and rotational signals in a single borehole is finally presented.

2. Simulation method and model setup

For the purpose of investigating the potential of rotational ground motions in oilfield applications, we calculate synthetic seismograms by using the ADER-DG method, the combination of a Discontinuous Galerkin finite element method and an Arbitrary high-order DERivative time integration approach developed by Dumbser and Käser, 2006. This method was extended to allow outputting the three components of rotation rate in addition to the three components of translational velocity.

The used model is a cube of 4680m sides: the Easting is from -2340m to 2340m, the Northing from -3140m to 1540m, and the depth stretches from –3840m to 840m. Receivers and sources (geometry suggested by Schlumberger) are located at the central area of the cube (Figure 1, Tables 1 & 2).

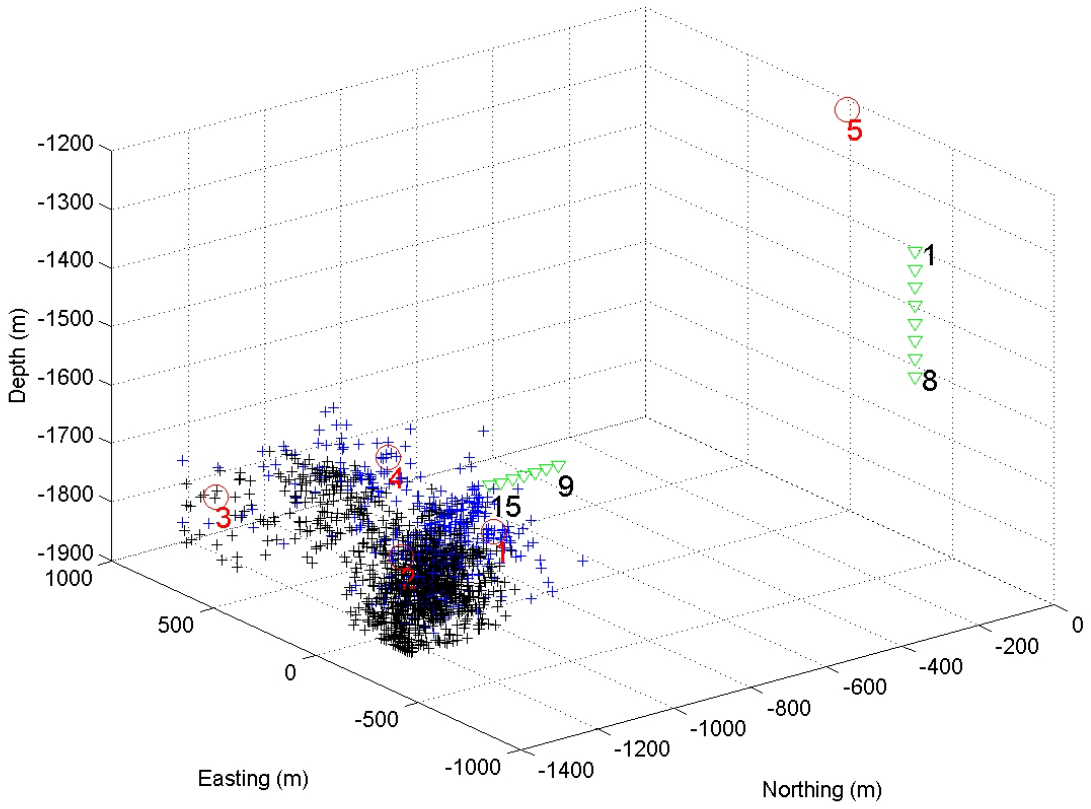

Figure 1. The geometrical setup for the locations of the sources and the receivers used in the simulations. Red circles (1 to 5): sources; Green triangles (1 to 15): receivers. Blue and black pluses: observed micro-seismic events.

Table 1. The locations of the receivers

Receiver index	Northing (m)	Easting (m)	Depth (m)	Receiver index	Northing (m)	Easting (m)	Depth (m)
1	-86.15	-478.45	-1365.06	9	-646.87	221.39	-1744.90
2	-86.09	-479.06	-1395.53	10	-677.34	220.82	-1745.20
3	-86.12	-479.68	-1426.01	11	-707.81	219.98	-1745.61
4	-86.25	-480.31	-1456.48	12	-738.27	219.32	-1746.03
5	-86.48	-480.94	-1486.95	13	-768.74	218.66	-1746.57
6	-86.81	-481.59	-1517.43	14	-799.22	218.21	-1746.50
7	-87.24	-482.25	-1547.89	15	-829.70	217.96	-1746.16
8	-88.67	-482.82	-1578.32				

Table 2. The locations of the sources

Source index	Northing (m)	Easting (m)	Depth (m)	Source index	Northing (m)	Easting (m)	Depth (m)
1	-1025	-169	-1729	4	-896	588	-1746
2	-1721	-173	-1729	5	-10	-4	-1213
3	-1340	604	-1739				

Table 3. The elastic parameters of the layered structure used in this study

Layer index from top to bottom	Thickness (m)	V_p (m/s)	V_s (m/s)	ρ (kg/m^3)
1	1680	6112	3127	2542
2	120	4210	2107	2357
3	120	3638	1744	2268
4	120	4864	2735	2463
5	120	3784	1987	2303
6	120	3049	1610	2185
7	120	3592	2076	2282
8	120	3049	1610	2185
9	120	3592	2076	2282
10	120	3784	1987	2303
11	120	4864	2735	2463
12	120	3638	1744	2268
13	120	4210	2107	2357
14	1560	6112	3127	2542

Two medium types are used. The first is a homogeneous medium with mass density ρ=2300 kg/m^3, and P and S wave velocities (respectively) are V_p= 3800m/s, V_s= 2000m/s. In this case, frequencies up to 15Hz are considered. The second is a layered structure that includes 14 horizontally parallel layers prepared for creating more realistic seismograms with scattering effects. The V_p, V_s and ρ used for the layered medium are taken based on the data provided by Schlumberger and presented in Table 3. In this case we consider frequencies up to about 30 Hz. The modeling parameters used for each case are detailed in Table 4.

The motions are originated by a double couple point source. The moment tensor $M = \begin{bmatrix} 0 & 0 & 1 \\ 0 & 0 & 0 \\ 1 & 0 & 0 \end{bmatrix}$ with strike=30 deg, dip=45 deg, rake=30 deg are applied for all simulations. The time dependent seismic moment rate used in this study is defined by equations (7), (8), and (9) presented in section 2.a - Part 1 of this report.

In total, we performed seven simulations: five simulations for the homogeneous medium with all source locations presented in Table 2 and two simulations for the layered structure with

sources situated at locations 1 and 5. Except the simulation for the source location 1 (Table 2, Figure 1) in the homogeneous medium implemented with $M_w \approx -4$, all the other simulations were carried out with $M_w = 0$. Here we note that seismograms can be scaled to arbitrary M_w within limits (see section 2.a - part 1).

Table 4. Modeling parameters used in the simulations

Modeling parameters	***Homogeneous medium***	***Layered structure***
Mesh type	Hexahedral	Hexahedral
Element edge length	65m	30 m
Total number of elements	373248	3796416
Polynomial order inside elements	4	5
Number of processors	128	256
Length of seismograms	1.25s	1.1s
Boundary condition	Absorbing	Absorbing
Minimum time step	$\sim 1.222 \times 10^{-3}$s	$\sim 1.6361 \times 10^{-4}$s
Run time per simulation	~ 1 hours	~ 36 hours

The simulation output data is written in files with names like Homo[fn1] ([fn2]).dat for the homogeneous medium and Layer[fn1] ([fn2]).dat for the layered structure. Here [fn1] indicates the source index, [fn2] indicates the receiver index (presented in Tables 1 and 2). For example, file Homo02 (15).dat stores the data of the simulation for the homogeneous medium, the source situated at location 2 obtained at receiver 15 (see Figure 1 and Tables 1 & 2).

An example of the simulated seismograms is given in Figure 2. The other synthetic seismograms can be found in the Appendix B (Figures B1-B5).

In the following, we proceed to the processing of the simulated seismograms. The processing studies focus on investigating the possible use of rotational ground motions to separate S from P waves, to estimate wave propagation directions and to determine S wave slowness.

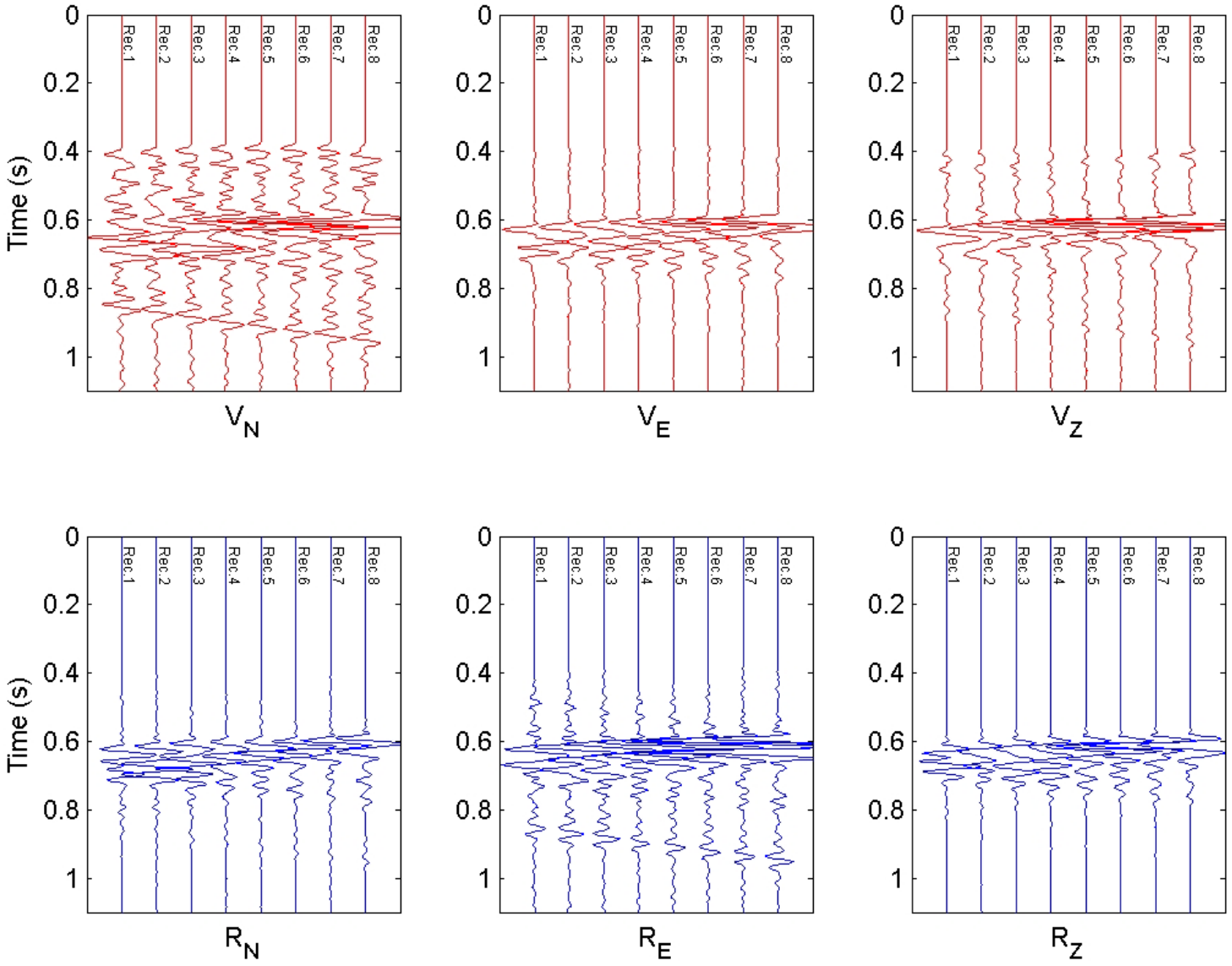

Figure 2. The simulated seismograms for the layered structure with source 1, obtained at the vertical profile (receivers 1 to 8). Top row: translation velocities. Bottom row: rotation rates.

3. Processing of synthetic seismograms

As we mentioned in the Part I of the report, one of the key questions is how joint measurements of rotations and translations can be used to provide more information about the wave field. Several answers were given in previous studies (e.g., Suryanto, 2007; Pham et al., 2009; Ferreira and Igel, 2009; Fichtner and Igel, 2009, Bernauer et al., 2009) and reviewed in Part I of this report. In the following, we present several ways to separate P and S waves and estimate propagation directions of S waves and S wave slowness using joint measurements of rotations and translations.

3.1. Separation of S and P waves

a) Direct comparison between accelerations and rotation rates

Theoretically, in a full space of a homogeneous isotropic medium, the wave forms in a window of S waves of any component of translational acceleration and any component of rotation rate induced by a point double-couple source are identical. It is because their wave forms are defined by the same source time function (see equations (1) and (3) in the Part I). In a previous study, Cochard et al. (2007) reported that under the assumption of plane wave propagation transverse acceleration and vertical rotation rate are in phase and their amplitudes are scaled by two times of apparent shear wave velocity. These properties can be used to constrain the appearance of S waves.

At first we examine the similarity of these seismograms in both homogeneous and layered structure cases. The Northing, Easting and vertical components of translational acceleration can be obtained by taking the time derivative of the corresponding components of the translational velocity outputted by the simulations. Transverse acceleration is inferred by rotating the Northing and Easting components of the acceleration in the Northing – Easting plane around the vertical axis a back-azimuth angle. The theoretical back-azimuth is defined here as the angle measured clock-wise from the Northing axis to the projection in the Northing – Easting plane of the line connected the receiver and the source locations. Examples of the superposition of the normalized accelerations and the normalized rotation rates are presented in Figures 3 and 4.

In Figure 3a we can recognize that for the homogeneous medium, the waveforms of the presented seismograms (i.e. translational accelerations and rotation rates) in the window of S waves are identical as we expected from theory. However, for the layered structure (Figure 3b) the waveforms of several components (e.g. vertical components of acceleration and rotation rate) are different. The differences are due to structure effects and the phenomenon can be seen as an indicator of scattering.

The superposition of the normalized transverse acceleration and the normalized vertical rotation rate presented in Figure 4 show very good fit between the two for both homogeneous and layered media. The apparent shear velocity thus can be estimated simply by taking half the ratio between the peak of the transverse acceleration and the peak of the vertical rotation rate. The obtained apparent velocities (Figures 4a, 4b) are as expected larger than the corresponding physical shear velocities (2000 m/s for homogeneous medium and 1610 m/s for the layer structure).

The direct comparison suggests the use of cross correlation techniques to separate S from P waves.

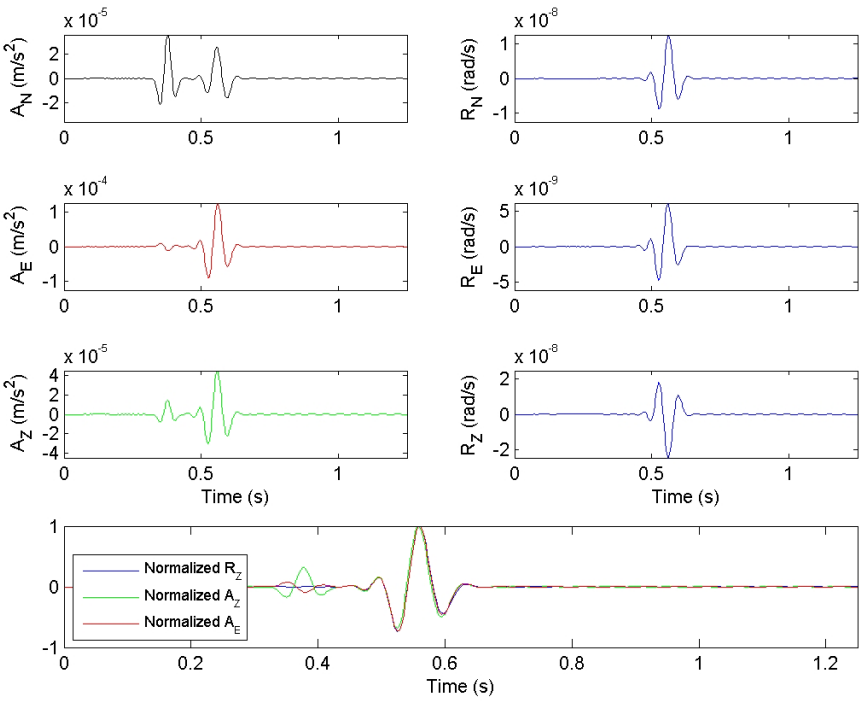

Figure 3. (a) Seismograms obtained at receiver 1 for the source situated at location 1 for the homogeneous medium. Top three traces on the left: Northing, Easting and vertical components of acceleration; Top three traces on the right: Northing, Easting and vertical components of rotation rate; Bottom: superposition of the normalized vertical and Easting accelerations and the normalized vertical rotation rate.

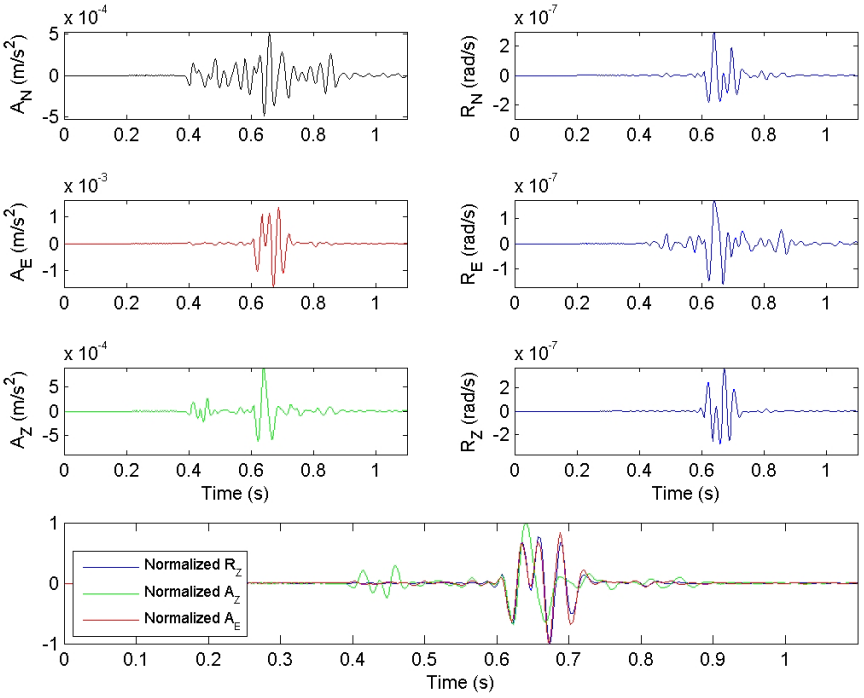

Figure 3. (b) Seismograms obtained at receiver 1 for the source situated at location 1 for the layered structure. Top three traces on the left: Northing, Easting and vertical components of acceleration; Top three traces on the right: Northing, Easting and vertical components of rotation rate; Bottom: superposition of the normalized vertical and Easting accelerations and the normalized vertical rotation rate.

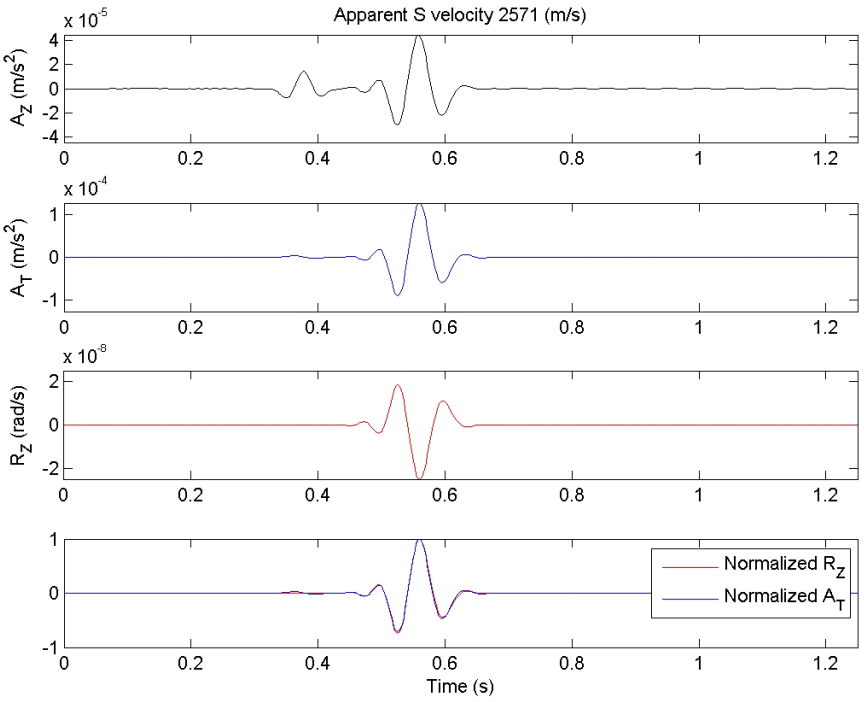

Figure 4. (a) Seismograms obtained at receiver 1 for the source situated at location 1 for the homogeneous medium. Top two traces: vertical and transverse components of acceleration; Third trace from top: vertical rotation rate; Bottom: superposition of the normalized transverse acceleration and the normalized vertical rotation rate.

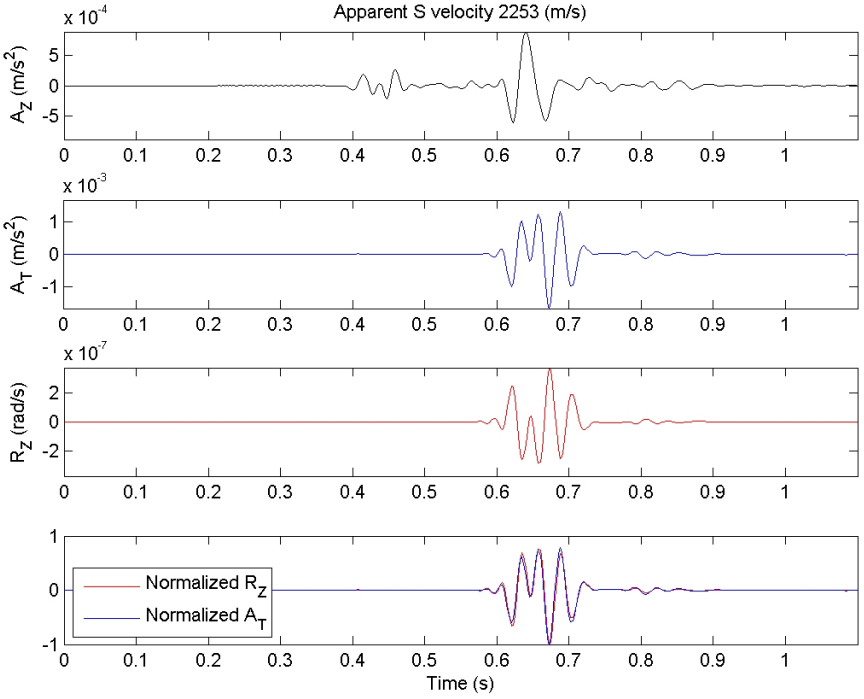

Figure 4. (b) Seismograms obtained at receiver 1 for the source situated at location 1 for the layered structure. Top two traces: vertical and transverse components of acceleration; Third trace from top: vertical rotation rate; Bottom: superposition of the normalized transverse acceleration and the normalized vertical rotation rate.

b) Cross correlation between transverse acceleration and vertical rotation rate

Since the waveforms of transverse acceleration and vertical rotation rate are almost identical in the window of S waves the cross correlation technique that allows quantifying the similarity of two seismograms in a sliding window might be a good tool to separate S waves. We examine this technique with synthetic seismograms of transverse acceleration and vertical rotation rate. Because the seismograms are output by numerical simulations, to constrain the normalized cross correlation at the signal sections we need to add random noise to the synthetic seismograms. In Figures 5a and 5b we show examples of the variations of the zero lag normalized cross-correlation coefficient between the vertical rotation rate and the transverse acceleration calculated for a sliding time window of appropriate length (twice the dominant period). Random noise with peak amplitude equal to three percent of the peak amplitude of the synthetic signals is added before calculating the correlation. Considering frequencies 15 Hz and 30 Hz respectively for cases of the homogeneous medium and the layered structure, high-pass filters with cut-off frequencies f = 15 Hz and f = 30 Hz, sliding time windows of 2/15 s and 2/30 s are applied respectively for the two studied cases. The sliding time step is taken by 0.1 times the sliding time window. We can see in the both cases presented in Figures 5a and 5b (bottom) that the correlation coefficient sharply increases when S waves are present. At the P coda and noise sections the correlation coefficients are much smaller. This phenomenon can be used to separate S from P waves.

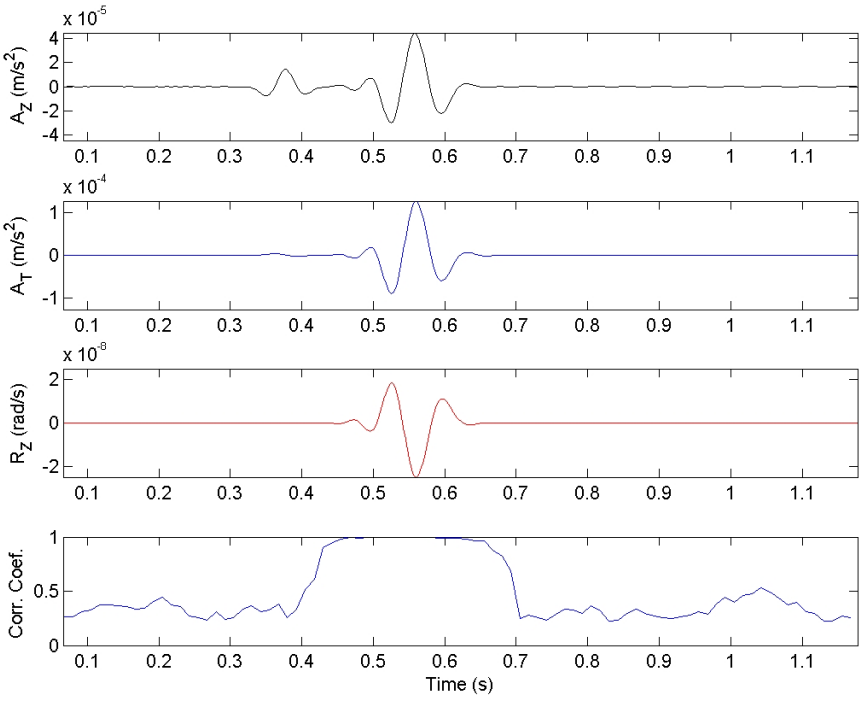

Figure 5. (a) Correlation between acceleration and rotation rate: Case study for the homogeneous medium, source location 1, receiver 1. Top two traces: vertical and transverse components of translation acceleration; Third trace from top: vertical rotation rate; Bottom: zero-lag normalized cross-correlation coefficients between rotation rate and transverse acceleration calculated for 2/15 s sliding time windows.

Before ending this section, we remind that in full space of a homogeneous isotropic medium the waveforms of any component of translational acceleration and any component of rotation rate induced by a point double-couple source for S waves are defined by the source time function and are always identical theoretically. In practice this may not work because of structure effects as we show in Figure 3 (b). However, the correlation between acceleration and rotation rate is insensitive with back azimuth and therefore we can not use their waveform comparison to constrain this parameter.

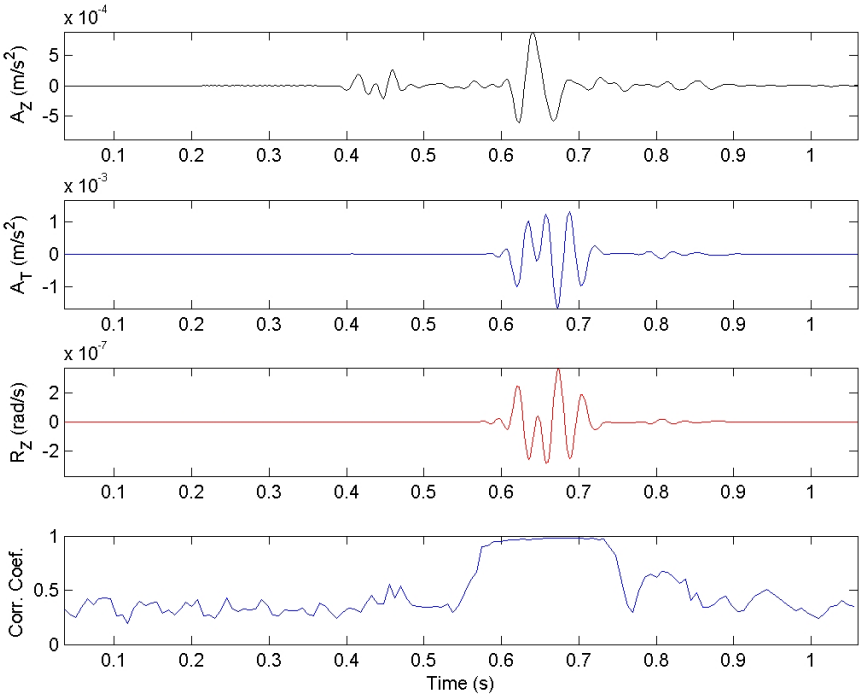

Figure 5. (b) Correlation between acceleration and rotation rate: Case study for the layered structure, source location 1, receiver 1. Top two traces: vertical and transverse components of translation acceleration; Third trace from top: vertical rotation rate; Bottom: zero-lag normalized cross-correlation coefficients between rotation rate and transverse acceleration calculated for 2/30 s sliding time windows.

c) Time dependence of rotation rate energy

In theory, the energy of rotational motions should be zero at the window of P waves and just appear when the S waves arrive. Thus we can also use this character to separate S from P. Because of the sensitivity with both P and S waves, the energy of translational acceleration (to be identical in the wave form with the energy of the corresponding rotation rate in the window of S waves as indicated by equation (13) in Part I) can not help in this problem.

We examine this idea by investigating the time dependence of energy of rotation rate E_{r} and energy of translational acceleration E_{a}. We define

$$E_{\mathrm{r}} = R_{\mathrm{N}}^2 + R_{\mathrm{E}}^2 + R_{\mathrm{Z}}^2 \tag{1}$$

$$E_{\mathrm{a}} = A_{\mathrm{N}}^2 + A_{\mathrm{E}}^2 + A_{\mathrm{Z}}^2 \tag{2}$$

where R_{N}, R_{E}, R_{Z}, and A_{N}, A_{E}, A_{Z} respectively are Northing, Easting and vertical components of rotation rate and translational acceleration.

Illustrations for time dependent variations of the energy are given in Figures 6a, 6b. The figures show that the onset of the energy of rotation rate coincides with the arrival time of S wave in both homogeneous and layered structure cases. Thus, variations of the energy of rotation rate also allow us constraining the appearance of S waves.

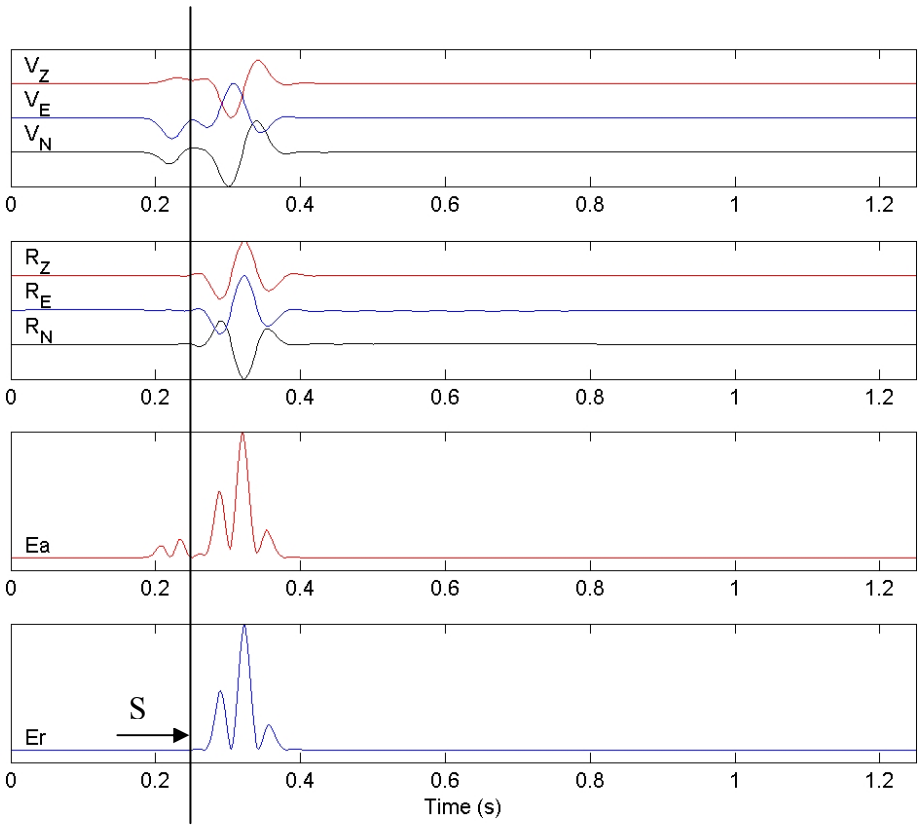

Figure 6. a) The separation of P and S waves: case study for the homogeneous medium, source location 1, receiver 11. Top six traces: vertical, Easting, and Northing components of translation velocity and rotation rate; Second trace from bottom: variation of the energy of translational acceleration; Bottom: variation of the energy of rotation rate. Note that all the traces are normalized. The onset of the energy of rotation rate indicates the arrival time of S wave.

Now it is fair to say that joint measurements of rotations and translations allow us separating S from P waves. Under the assumption of plane wave propagation, the similarity of the waveforms of transverse acceleration and vertical rotation rate is consistent. Thus, the method to constrain the appearance of S waves using the waveform comparison is more stable in case where transverse acceleration and vertical rotation rate are used. This implies that the back azimuth needs to be known. However, the waveform comparison method based on the cross correlation technique by itself can not provide the back azimuth information. This raises the motivation for us to proceed in quantifying this parameter (i.e. back-azimuth) by using other approaches that will be presented in the following section.

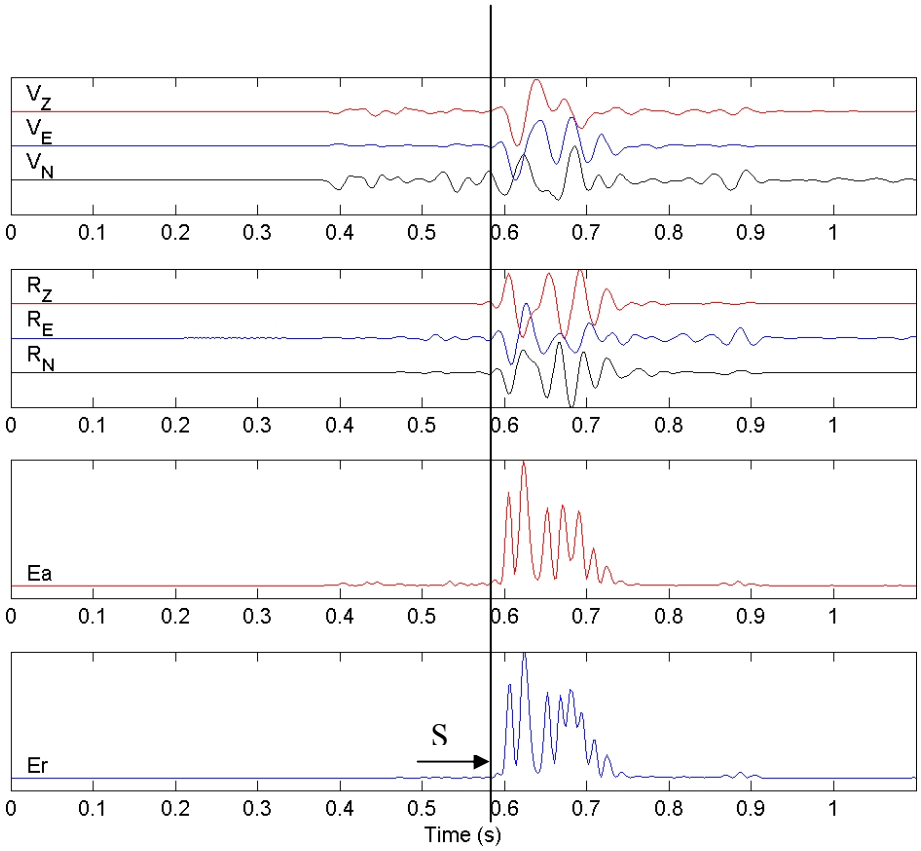

Figure 6. b) The separation of P and S waves: case study for the layered structure, source location 1, receiver 3. Top six traces: vertical, Easting, and Northing components of translation velocity and rotation rate; Second trace from bottom: variation of the energy of translational acceleration; Bottom: variation of the energy of rotation rate. Note that all the traces are normalized. The onset of the energy of rotation rate indicates the arrival time of S wave.

3.2. *Estimation of S-wave propagation directions using the polarizations of S-wave motions*

Theoretically, in an isotropic medium if S waves propagate along $\mathfrak{R}$ direction, their rotational and translational signals will polarize along two perpendicular axes those in combination with $\mathfrak{R}$ axis create an orthogonal system. This can be inferred from radiation patterns of translational and rotational motions shown in part I (equation (3) and (6)). Thus, the propagation direction of an S wave can be estimated by taking the cross product of the particle polarizations of its translational and rotational motions.

From the estimated propagation direction, back-azimuth φ_S and incidence angle i_S of the S wave can be extracted. The back-azimuth φ_S is determined by the angle between the unit vector $\mathbf{N}$ $\{1, 0, 0\}$ of the Northing axis and the projection $\mathfrak{R}^{xy}$ $\{-\mathfrak{R}_x, -\mathfrak{R}_y, 0\}$ of the backward propagation direction of the S wave in the Northing – Easting plane (measured clock-wise from $\mathbf{N}$ to $\mathfrak{R}^{xy}$). This angle can be calculated exactly by using definitions of dot and cross products

$$\varphi_S = \arccos\frac{-\mathfrak{R}_x}{\sqrt{\mathfrak{R}_x^2 + \mathfrak{R}_y^2}} * \frac{180}{\pi} \qquad \text{(deg.) if} \qquad \mathfrak{R}_y < 0 \qquad \text{(3a)}$$

$$\varphi_S = 360 - \arccos\frac{-\Re_x}{\sqrt{\Re_x^2 + \Re_y^2}} * \frac{180}{\pi} \text{ (deg.) if } \quad \Re_y \geq 0 \tag{3b}$$

In the case where it is unclear if the propagation direction $\mathfrak{R}\{\Re_x, \Re_y, \Re_z\}$ is backward or forward we define the azimuth ψ_S of the S wave by the angle between $\mathbf{N}$ $\{1, 0, 0\}$ and $\mathfrak{R}^{xy}$ $\{\Re_x, \Re_y, 0\}$

$$\psi_S = \arccos\frac{\Re_x}{\sqrt{\Re_x^2 + \Re_y^2}} * \frac{180}{\pi} \text{ (deg.)} \tag{4}$$

The incidence angle i_S is determined by the angle between the unit vector $\mathbf{Z}$ $\{0, 0, 1\}$ of the vertical axis and the propagation direction $\mathfrak{R}$ $\{\Re_x, \Re_y, \Re_z\}$ of the S wave

$$i_S = \arccos\frac{\Re_z}{\sqrt{\Re_x^2 + \Re_y^2 + \Re_z^2}} * \frac{180}{\pi} \text{ (deg.)} \tag{5}$$

We use the synthetic seismograms to test this approach. At each receiver, in a considered time window we determine the polarizations $\mathbf{P}_{\mathrm{tS}}$ and $\mathbf{P}_{\mathrm{rS}}$ of translational and rotational motions of S waves, respectively, by using three components of translational accelerations and three components of rotation rates weighted by amplitudes of the energy of the corresponding rotation rate (to avoid the involvements of P waves)

$$\mathbf{P}_{\mathrm{tS}} = \mathbf{A}\ \{A_{\mathrm{N}}, A_{\mathrm{E}}, A_{\mathrm{Z}}\} * E_{\mathrm{r}} \tag{6}$$

$$\mathbf{P}_{\mathrm{rS}} = \mathbf{R}\ \{R_{\mathrm{N}}, R_{\mathrm{E}}, R_{\mathrm{Z}}\} * E_{\mathrm{r}} \tag{7}$$

A time window sliding along the whole time series of a certain event is used here. At first, for each time window only one sample at the time when the corresponding E_{r} reaches its peak value is considered. For this test, the polarizations $\mathbf{P}_{\mathrm{tS}}$ and $\mathbf{P}_{\mathrm{rS}}$ are modified by

$$\mathbf{P}_{\mathrm{tS}} = \mathbf{A}\ \{A_{\mathrm{N}}, A_{\mathrm{E}}, A_{\mathrm{Z}}\} * E_{\mathrm{r}} * \Pi_{\mathrm{a,b}} \tag{8}$$

$$\mathbf{P}_{\mathrm{rS}} = \mathbf{R}\ \{R_{\mathrm{N}}, R_{\mathrm{E}}, R_{\mathrm{Z}}\} * E_{\mathrm{r}} * \Pi_{\mathrm{a,b}} \tag{9}$$

where $\Pi_{\mathrm{a,b}}$ is a boxcar function with both a and b are coincided with the time when the E_{r} reaches its peak value in the considered time window.

The forward propagation direction $\mathfrak{R}$ is determined by nonzero vector of the cross product of $\mathbf{P}_{\mathrm{rS}}$ and $\mathbf{P}_{\mathrm{tS}}$ defined by (8) and (9). The back azimuth and incidence angle of the S wave in each time window are extracted using equations (3) and (5). The time window length of a predominant period (1/30 s for the homogeneous medium and 1/15 s for the layered structure) and the sliding step of half the predominant period are used. The presence of energy of rotation rate is used to constrain the appearance of S waves. Only the windows in which the corresponding peak energy of rotation rate is greater than or equal to one percent of the peak energy of rotation rate in the whole time series are chosen to apply the polarization approach. Typical results are shown in Figures 7a, 7b. We can see that for the homogeneous medium (Figure 7a) the estimated back-azimuths and incidence angles of S waves in different time windows almost coincide exactly with the theoretical values calculated from known locations of the source and receiver. We note that the theoretical incidence angle is defined here as the angle between the unit vector $\mathbf{Z}$ $\{0, 0, 1\}$ of the vertical axis and the

line connected the source and the receiver locations. The result implies that the approach works well. For the layer structure case (Figure 7b), the estimated incidence angles of S waves in several windows are different from the theoretical value. It indicates that S waves in those windows are not direct S waves but refracted or reflected ones at the layered surfaces. However, the estimated back-azimuths in almost windows are still unchanged and coincide with the theoretical ones.

In practice to avoid the uncertainty caused by unexpected noise we can take into account all samples in the considering time window. For this case, we use the cross product of $\mathbf{P}_{\mathrm{rS}}$ and $\mathbf{P}_{\mathrm{tS}}$ given by (6) and (7) to define propagation direction $\mathfrak{R}$ for every sample in the considered time window. We then estimate azimuth ψ_S^i and incidence angle i_S^i for any i-th sample in the considered time window using equations (4) and (5). The azimuth ψ_S and incidence angle i_S for the S wave in the considering time window is calculated by

$$\psi_S = \frac{\sum_{i=1}^{n} k^i \psi_S^i}{\sum_{i=1}^{n} k^i} \tag{10}$$

$$i_S = \frac{\sum_{i=1}^{n} k^i i_S^i}{\sum_{i=1}^{n} k^i} \tag{11}$$

where $k^i = \frac{\left(R_N^i\right)^2 + \left(R_E^i\right)^2 + \left(R_Z^i\right)^2}{E_r^{\min}}$, $E_r^{\min}$ is minimum value of E_{r} in the considering time window.

We again test this solution by using the synthetic data. The time window length of a predominant period (1/30 s for the homogeneous medium and 1/15 s for the layered structure) and the sliding step of half the predominant period are still used. Also, only the windows that the corresponding peak energy of rotation rate is greater than or equal to one percent of the peak energy of rotation rate in the whole time series are considered. The typical obtained results shown in Figures 8a, 8b again demonstrate that this solution work well. The results are very similar to the illustrations given in Figure 7a, 7b except we do not know if the propagation direction of the S wave is backward or forward.

We now examine back-azimuths estimated by the polarization approach for all cases of the sources, receivers, and medium types used in the simulations. Here, only one window that covers the whole the time series and one sample at the time when the corresponding E_{r} reaches its peak value is considered. The differences between the estimated back-azimuths and the theoretical ones are calculated and presented in Figure 9. With the maximum error of about 7 degrees for the layered structure and of about 2 degrees for the homogeneous medium, the method is revealed as a very powerful tool for back-azimuth estimations.

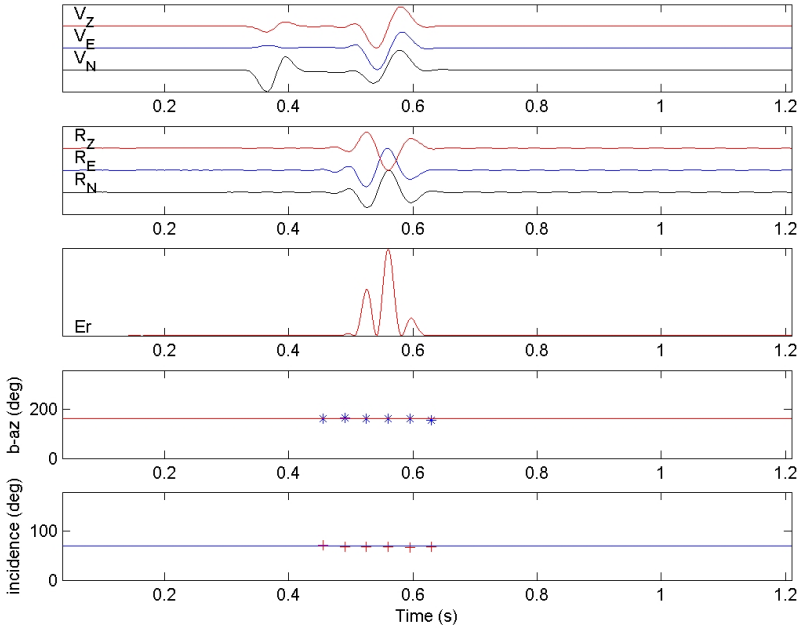

Figure 7. a) Back-azimuths and incidence angles estimated from the polarizations of S waves for sliding windows: case study for **the homogeneous medium, source 1, receiver 1,** only one sample in each sliding time window is considered. Top six traces: vertical, Easting, and Northing components of translation velocity and rotation rate; Third trace from bottom: variation of the energy of rotation rate. Note that all the traces are normalized. Blue stars (second box from bottom): back-azimuths estimated from the polarizations of S waves for sliding windows. Red line indicates the theoretical back-azimuth; Bottom (red pluses): incidence angles estimated from the polarizations of S waves for sliding windows. Blue line indicates the theoretical incidence.

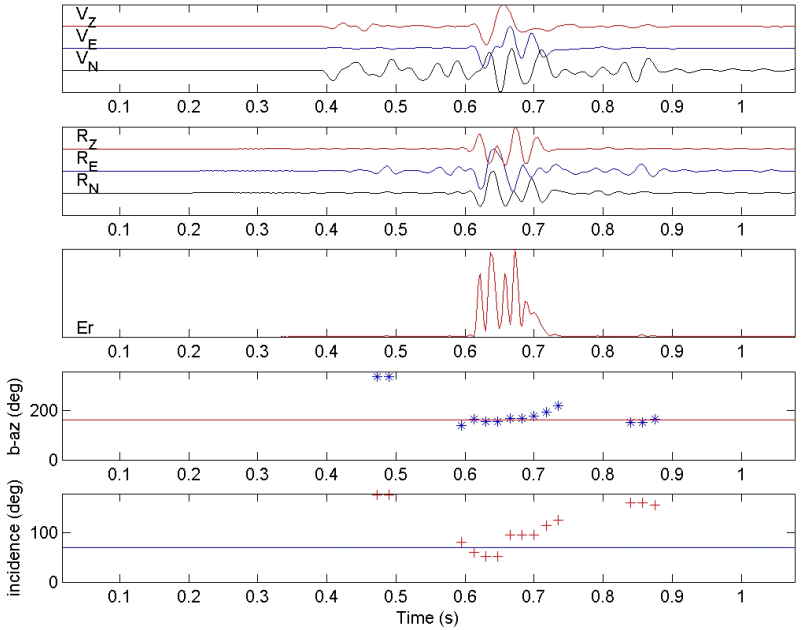

Figure 7. b) Back-azimuths and incidence angles estimated from the polarizations of S waves for sliding windows: case study for the **the layered structure, source location 1, receiver 1,** only one sample in each sliding time window is considered. Top six traces: vertical, Easting, and Northing components of translation velocity and rotation rate; Third trace from bottom: variation of the energy of rotation rate. Note that all the traces are normalized. Blue stars (second box from bottom): back-azimuths estimated from the polarizations of S waves for sliding windows. Red line indicates the theoretical back-azimuth; Bottom (red pluses): incidence angles estimated from the polarizations of S waves for sliding windows. Blue line indicates the theoretical incidence.

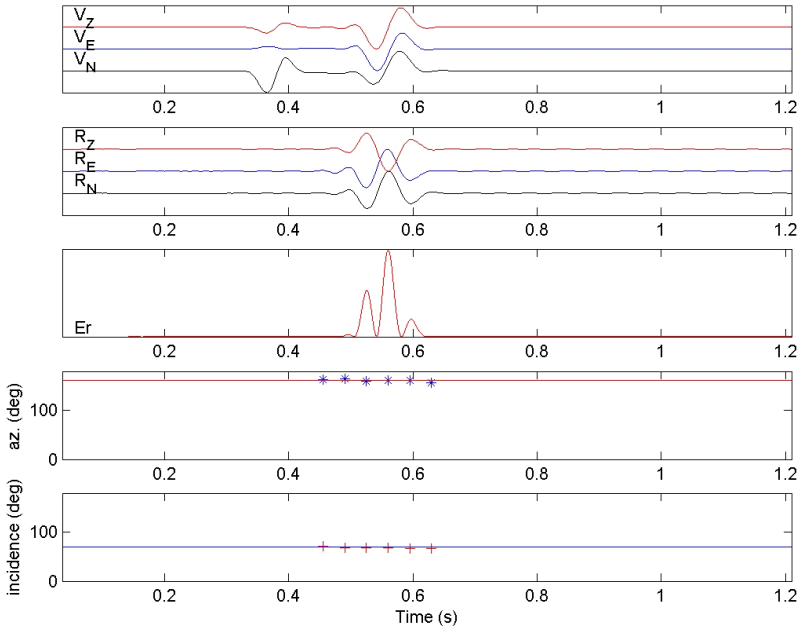

Figure 8. a) Azimuths and incidence angles estimated from the polarizations of S waves for sliding windows: case study for **the homogeneous medium, source location 1, receiver 1,** all samples in each sliding time window are taken into account. Top six traces: vertical, Easting, and Northing components of translation velocity and rotation rate; Third trace from bottom: variation of the energy of rotation rate. Note that all the traces are normalized. Blue stars (second box from bottom): azimuths estimated from the polarizations of S waves for sliding windows. Red line indicates the theoretical azimuth; Bottom (red pluses): incidence angles estimated from the polarizations of S waves for sliding windows. Blue line indicates the theoretical incidence.

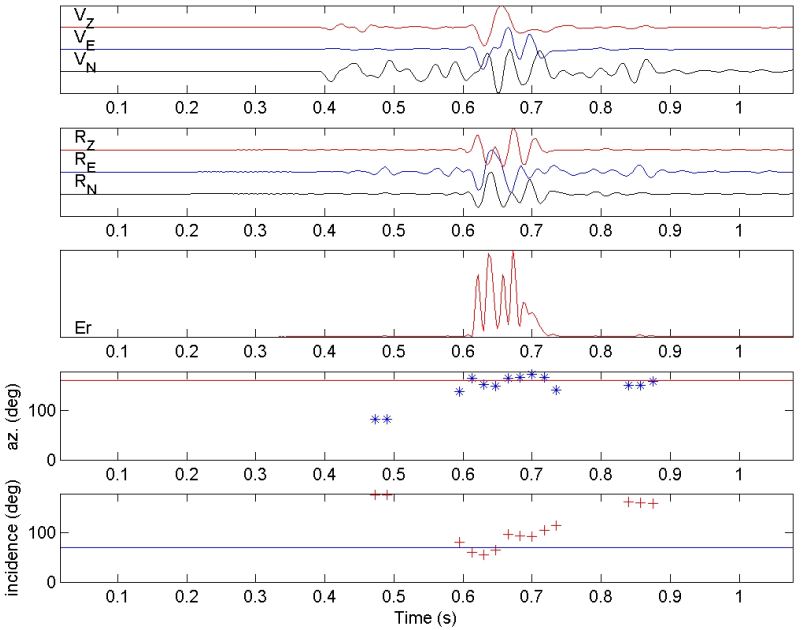

Figure 8. b) Azimuths and incidence angles estimated from the polarizations of S waves for sliding windows: case study for the **the layered structure, source location 1, receiver 1,** all samples in each sliding time window are taken into account. Top six traces: vertical, Easting, and Northing components of translation velocity and rotation rate; Third trace from bottom: variation of the energy of rotation rate. Note that all the traces are normalized. Blue stars (second box from bottom): azimuths estimated from the polarizations of S waves for sliding windows. Red line indicates the theoretical azimuth; Bottom (red pluses): incidence angles estimated from the polarizations of S waves for sliding windows. Blue line indicates the theoretical incidence.

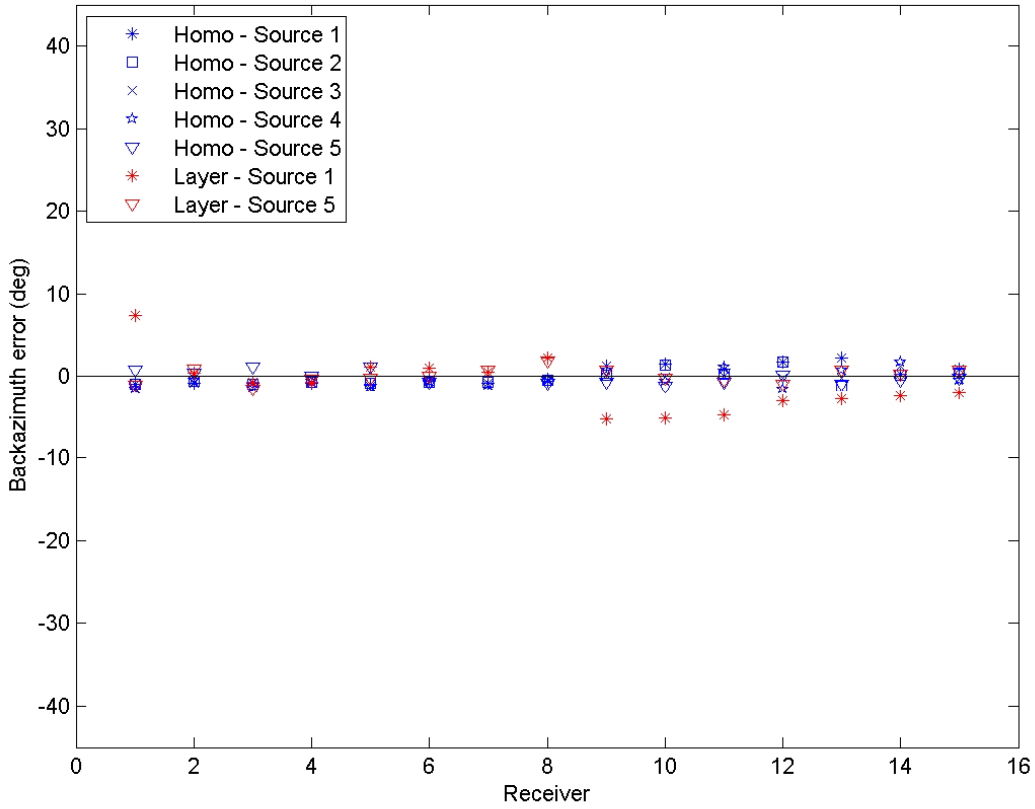

Figure 9. Differences between the back-azimuths estimated from the polarizations of S waves and the theoretical back-azimuths for all used sources and receivers.

3.*3. Estimation of S-wave slowness*

In case several 6 component receivers are deployed in a borehole it is possible to calculate the slowness vectors of S waves. This calculation may provide information of not only wave propagation directions but also anisotropy (Horne, personal communication). In the following we present the theory to estimate S-wave slowness using joint measurements of rotational and translational motions at linear receivers, then we use the synthetic seismograms to test back-azimuths and incidence angles extracted from the estimated slowness vectors.

a) Theory

In seismology, rotation rates $\mathbf{R}$ are defined by half of the curl of the translational velocity field $\mathbf{V}$

$$\mathbf{R} = \frac{1}{2}\nabla \times \mathbf{V} \tag{12}$$

$$R_x = \frac{1}{2}\left(\frac{\partial V_z}{\partial y} - \frac{\partial V_y}{\partial z}\right) \tag{13}$$

$$R_y = \frac{1}{2}\left(\frac{\partial V_x}{\partial z} - \frac{\partial V_z}{\partial x}\right) \tag{14}$$

$$R_z = \frac{1}{2}\left(\frac{\partial V_y}{\partial x} - \frac{\partial V_x}{\partial y}\right) \tag{15}$$

For plane waves

$$\mathbf{V} = \mathbf{v}e^{i\omega(t-\mathbf{S}\bullet\mathbf{X})} \tag{16}$$

where $\mathbf{S}$ is the slowness vector.

Thus

$$\begin{aligned}\frac{\partial V_z}{\partial y} &= -i\omega S_y V_z \\ &= -A_z S_y\end{aligned} \tag{17}$$

Here $\mathbf{A}$ is translational acceleration.

Similarly

$$\frac{\partial V_y}{\partial z} = -A_y S_z \tag{18}$$

$$\frac{\partial V_x}{\partial z} = -A_x S_z \tag{19}$$

$$\frac{\partial V_z}{\partial x} = -A_z S_x \tag{20}$$

$$\frac{\partial V_y}{\partial x} = -A_y S_x \tag{21}$$

$$\frac{\partial V_x}{\partial y} = -A_x S_y \tag{22}$$

In the case that receivers are deployed in a vertical borehole, the vertical component of the slowness vector can be inferred from (18)

$$S_z = -\frac{1}{A_y}\frac{\partial V_y}{\partial z} \approx -\frac{1}{A_y}\frac{\Delta V_y}{\Delta z} \tag{23}$$

or can be inferred from (19)

$$S_z = -\frac{1}{A_x}\frac{\partial V_x}{\partial z} \approx -\frac{1}{A_x}\frac{\Delta V_x}{\Delta z} \tag{24}$$

The combinations of (13), (17), and (18) and (14), (19), and (20) lead to

$$S_y = \frac{1}{A_z}\left(A_y S_z - 2R_x\right) \tag{25}$$

$$S_x = \frac{1}{A_z}\left(A_x S_z + 2R_y\right) \tag{26}$$

In the case that receivers are deployed in a horizontal borehole along x axis, the x component of the slowness vector can be inferred from (20)

$$S_x = -\frac{1}{A_z}\frac{\partial V_z}{\partial x} \approx -\frac{1}{A_z}\frac{\Delta V_z}{\Delta x} \tag{27}$$

or can be inferred from (21)

$$S_x = -\frac{1}{A_y}\frac{\partial V_y}{\partial x} \approx -\frac{1}{A_y}\frac{\Delta V_y}{\Delta x} \tag{28}$$

The combinations of (14), (19), and (20) and (15), (21), and (22) lead to

$$S_z = \frac{1}{A_x}\left(A_z S_x - 2R_y\right) \tag{29}$$

$$S_y = \frac{1}{A_x}\left(A_y S_x + 2R_z\right) \tag{30}$$

Equations (25), (26), (29), and (30) indicate that the method will not work if S waves propagate along the monitoring borehole.

b) Back-azimuth estimation using S-wave slowness

Similar to the calculations in section 3.2, we can estimate the back-azimuth φ_S and the incidence angle i_S from the slowness vector $\mathbf{S}$ $\{S_x, S_y, S_z\}$

$$\varphi_S = \arccos\frac{-S_x}{\sqrt{S_x^2 + S_y^2}} * \frac{180}{\pi} \text{ (deg.) if } \quad S_y < 0 \tag{31a}$$

$$\varphi_S = 360 - \arccos\frac{-S_x}{\sqrt{S_x^2 + S_y^2}} * \frac{180}{\pi} \text{ (deg.) if } \quad S_y \geq 0 \tag{31b}$$

$$i_S = \arccos\frac{S_z}{\sqrt{S_x^2 + S_y^2 + S_z^2}} * \frac{180}{\pi} \quad \text{(deg.)} \tag{32}$$

We use the synthetic seismograms obtained at receivers 1 to 8 in the vertical borehole to examine the method for both cases of the homogeneous medium and the layered structure. At each receiver location, we use the aforementioned equations to calculate back-azimuths and incidence angles for sliding time windows and compare them with the theoretical ones. The presence of energy of rotation rate is used to constrain the appearance of S waves. Only the windows where the corresponding peak energy of rotation rate is greater than or equal to one percent of the peak energy of rotation rate in the whole time series are chosen to apply the slowness approach. For each sliding time window, the mean values of the considered components (e.g. A_x, A_y, A_z) are used for calculations. The vertical component of slowness vector S_z is averaged from equations (23) and (24). The typical obtained results for the sliding window length of 0.2 times predominant period T (T=1/30 s for the homogeneous medium and T=1/15 s for the layered structure) and the sliding step of half the window length are presented in Figure 10. The figure shows that for case of the homogeneous medium the method works efficiently. However, for the layered structure the obtained results are not consistent.

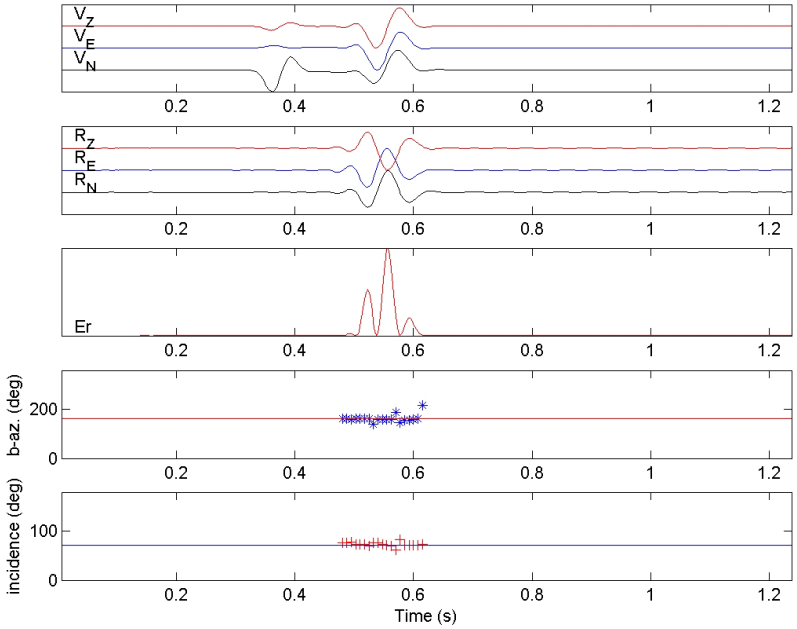

Figure 10. a) Back-azimuths and incidence angles estimated based on S-wave slowness for sliding windows: case study for **the homogeneous medium, source 1, receiver 2**. Top six traces: vertical, Easting, and Northing components of translation velocity and rotation rate; Third trace from bottom: variation of the energy of rotation rate. Note that all the traces are normalized. Blue stars (second box from bottom): estimated azimuths for sliding windows. Red line indicates the theoretical azimuth; Bottom (red pluses): estimated incidence angles for sliding windows. Blue line indicates the theoretical incidence.

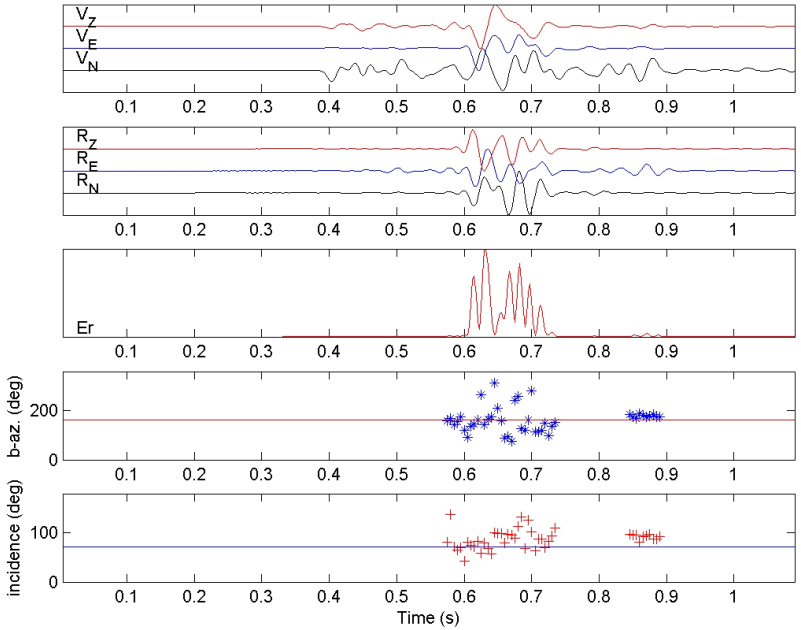

Figure 10. b) Back-azimuths and incidence angles estimated based on S-wave slowness for sliding windows: case study for **the layered structure, source 1, receiver 2**. Top six traces: vertical, Easting, and Northing components of translation velocity and rotation rate; Third trace from bottom: variation of the energy of rotation rate. Note that all the traces are normalized. Blue stars (second box from bottom): estimated azimuths for sliding windows. Red line indicates the theoretical azimuth; Bottom (red pluses): estimated incidence angles for sliding windows. Blue line indicates the theoretical incidence.

We finally test the differences between back-azimuths estimated by the slowness approach and the corresponding theoretical values for all cases of the sources, receivers, and medium types used in the simulations. The sliding window length of 0.2 times predominant period T (T=1/30 s for the homogeneous medium and T=1/15 s for the layered structure) and the sliding step of half the window length are used. For each case, the back-azimuth value obtained at the window where the corresponding E_r reaches its maximum value is taken to compare with the theoretical back-azimuth. The results are presented in Figure 11. We can see that with source location 5, the method does not work satisfactory even for the homogeneous medium. This is because the signals of vertical components of translational motions of S waves in this case are very weak (S waves propagate almost along the vertical borehole). This is the limit of the method mentioned before in section (3.3.a). For the other cases in homogeneous medium the slowness method provides satisfactory results with the maximum error of about 4 degrees. For the layered structure case the results are not consistent.

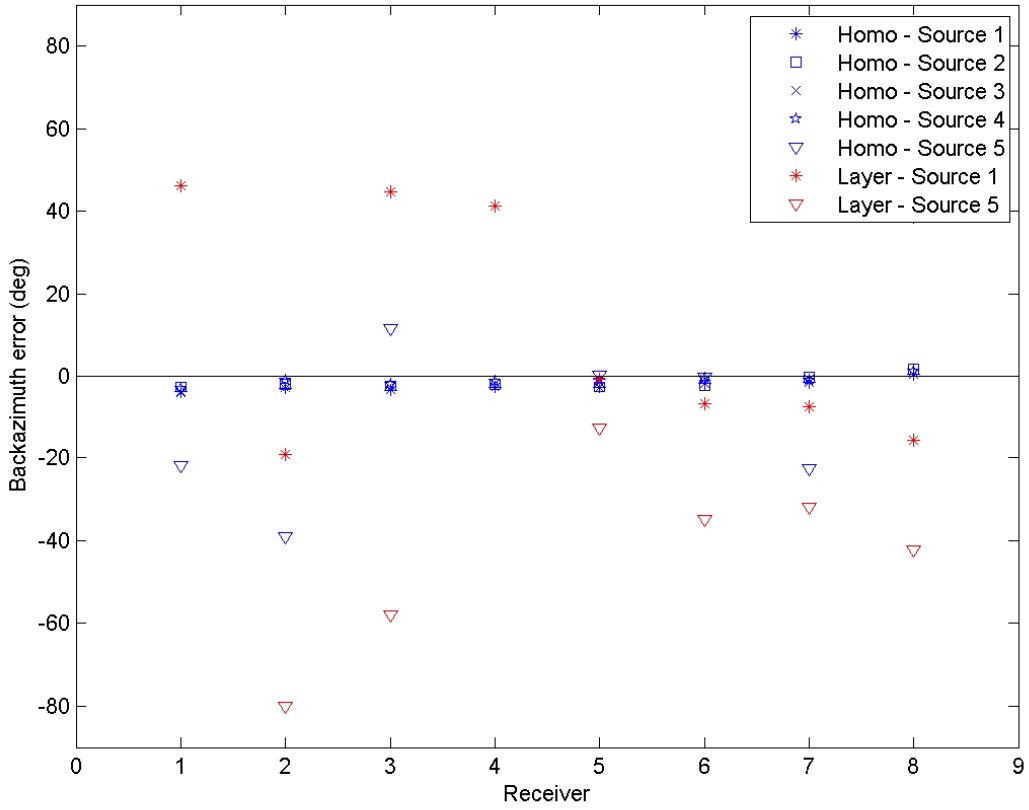

Figure 11. Differences between the back-azimuths estimated from the S-wave slowness and the theoretical back-azimuths for receivers 1-8 in the vertical borehole.

4. Conclusions and recommendations

In this report we present the updated progress in using rotational ground motions for oilfield applications. Here we summarize the results and formulate some recommendations for specific applications and further studies.

The key results and recommendations are:

- The (additional) measurement of rotational ground motions allows the separation of P- and S-wave energy. For this purpose, either time dependence of rotation rate energy or cross correlation between translational acceleration and rotation rate can be used. For complicated seismograms these might facilitate the identification of shear phases.
- In full space of a homogeneous isotropic medium the waveforms of any component of translational acceleration and any component of rotation rate induced by a point double-couple source for S waves are always identical in theory. Thus, the correlation between acceleration and rotation rate is insensitive with back azimuth and we can not use their waveform comparison to constrain this parameter. However, one can use this character to investigate scattering properties.
- In isotropic material, propagation direction of S waves (back azimuth and incidence angle) can be estimated by taking the cross product of the polarizations of translational and rotational motions. This method requires 6 component measurements at only one point.
- Joint measurements of both translational and rotational ground motions at a linear array of borehole receivers allow us to estimate S-wave slowness. Although the wave propagation direction extracted from the estimated S-wave slowness is worse compared to the results of the polarization method, especially for complicated media, the S-wave slowness method works in anisotropic media and provides more information about anisotropy. The method is limited when S waves propagate along the monitoring borehole.
- Determination of wave propagation direction opens another opportunity to investigate scattering properties using variations of rotational motions around radial axis that should be zero in homogeneous isotropic media.

References

Bernauer, M., Fichtner, A., Igel, H., Inferring near-receiver structure from combined measurements of rotational and translational ground motions, Geophysics, submitted (2009).

Bernauer, M., Tomography with rotations, Diploma Thesis LMU Munich, 2009.

Cochard, A., Igel, H., Schuberth, B., Suryanto, W., Velikoseltsev, A., Schreiber, U., Wassermann, J., Scherbaum, F., Vollmer, D. Rotational motions in seismology: theory, observations, simulation, in "*Earthquake source asymmetry, structural media and rotation effects*" eds. Teisseyre et al., Springer Verlag (2006).

Dumbser, M., and Käser. M. An arbitrary high order discontinuous Galerkin method for elastic waves on unstructured meshes II: The three-dimensional isotropic case, *Geophys. J. Int.*, *167*(1), 319-336, doi:10.1111/j.1365-246X.2006.03120.x. (2006).

Eisner, L., Fischer, T., and Rutledge T. J. Determination of S-wave slowness from a linear array of borehole receivers, *Geophys. J. Int.*, 176, 31-39, doi: 10.1111/j.1365-246X.2008.03939x, (2009).

Ferreira, A., Igel, H., Rotational motions of seismic surface waves in a laterally heterogeneous Earth, *Bull. Seism. Soc. Amer.*, v. 99; no. 2B; p. 1429-1436; DOI: 10.1785/0120080149 (2009).

Fichtner A. and Igel H., Sensitivity densities for rotational ground motion measurements, *Bull. Seism. Soc. Amer.*, v. 99; no. 2B; p. 1302-1314; DOI: 10.1785/0120080064 (2009).

Igel, H., Cochard, A., Wassermann, J., Flaws, A., Schreiber, U., Velikoseltsev, A., Pham, D.N. Broadband Observations of Earthquake Induced Rotational Ground Motions, *Geophys. J. Int.*, 168, 182-196, doi: 10.1111/j.1365-246X.2006.03146x, (2007).

Igel, H., Schreiber, K.U., Flaws, A., Schuberth, B., Velikoseltsev, A., Cochard, A., Rotational motions induced by the M8.1 Tokachi-oki earthquake, September 25, 2003, *Geophys. Res. Lett.*, 32, L08309, doi:10.1029/2004GL022336 (2005).

McLeod, D.P., Stedman, G.E., Webb, T.H. & Schreiber, U. Comparison of standard and ring laser rotational seismograms. *Bull. Seism. Soc. Amer.* 88, 1495-1503 (1998).

Pancha, A., Webb, T.H., Stedman, G.E., McLeod, D.P. & Schreiber, U. Ring laser detection of rotations from teleseismic waves. *Geophys. Res. Lett*. 27, 3553-3556 (2000).

Pham D.N., Igel H., Wassermann, J., M. Käser, J. de la Puente, Schreiber, U. Observations and modelling of rotational signals in the P-Coda: constraints on crustal scattering, *Bull. Seism. Soc. Amer.*, v. 99; no. 2B; p. 1315-1332; DOI: 10.1785/0120080101 (2009a).

Pham, D.N., Igel H., Wassermann, J., Schreiber, U., A. Cochard, The effects of tilt on interferometric rotation sensors, *Bull. Seism. Soc. Amer.*, v. 99; no. 2B; p. 1352-1365; DOI: 10.1785/0120080181 (2009b).

Schreiber, U., J. N. Hautmann, A. Velikoseltsev, J. Wassermann, H. Igel, J. Otero, F. Vernon, and J.-P. R. Wells, Ring Laser Measurements of Ground Rotations for Seismology, Bull. Seis. Amer. Soc., v. 99; no. 2B; p. 1190-1198; DOI: 10.1785/0120080171 (2009).

Schreiber, U., Stedman, G.E., Igel, H., Flaws, A. Ring laser gyroscopes as rotation sensors for seismic wave studies. In "*Earthquake source asymmetry, structural media and rotation effects*" eds. Teisseyre et al., Springer Verlag (2006).

Suryanto, W., J. Wassermann, H. Igel, A. Cochard, D. Vollmer, F. Scherbaum, A. Velikoseltsev, and U. Schreiber. First comparison of seismic array derived rotations with direct ring laser measurements of rotational ground motion, Bull. Seism. Soc. Am., 96(6), 2059-2071, doi:10.1785/0120060004 (2006).

Suryanto, W. Rotational Motions in Seismology: Theory and Application. Dissertation, LMU München: Fakultät für Geowissenschaften (2006).

Wassermann, J., S. Lehndorfer, H. Igel, U. Schreiber. Performance test of a commercial rotational motion sensor, Bull. Seism. Soc. Amer., v. 99; no. 2B; p. 1449-1456; DOI: 10.1785/0120080157 (2009).

Appendix B:

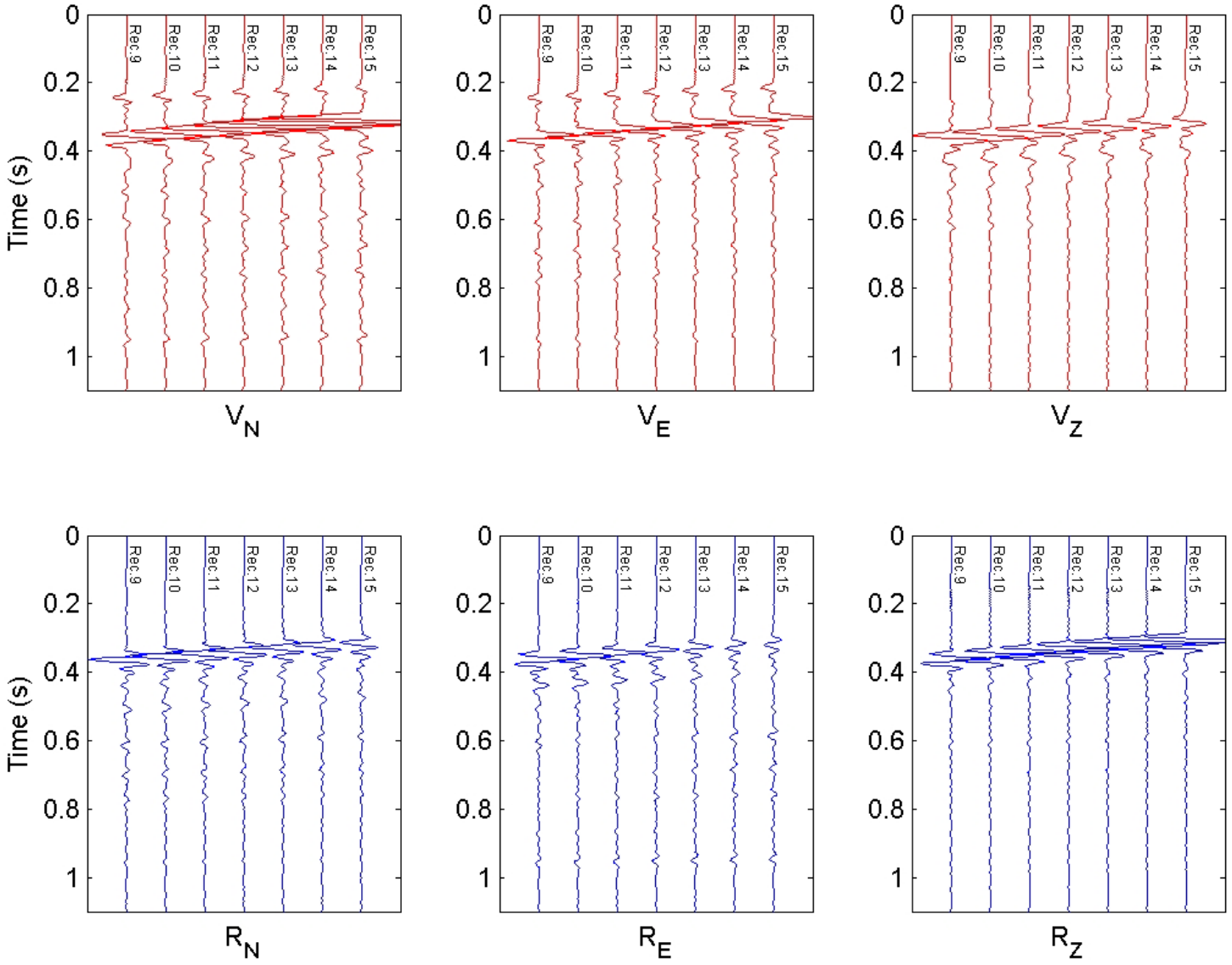

Figure B1. The simulated seismograms for the layered structure with source 1, obtained at the horizontal profile (receivers 9 to 15). Top row: translation velocities. Bottom row: rotation rates.

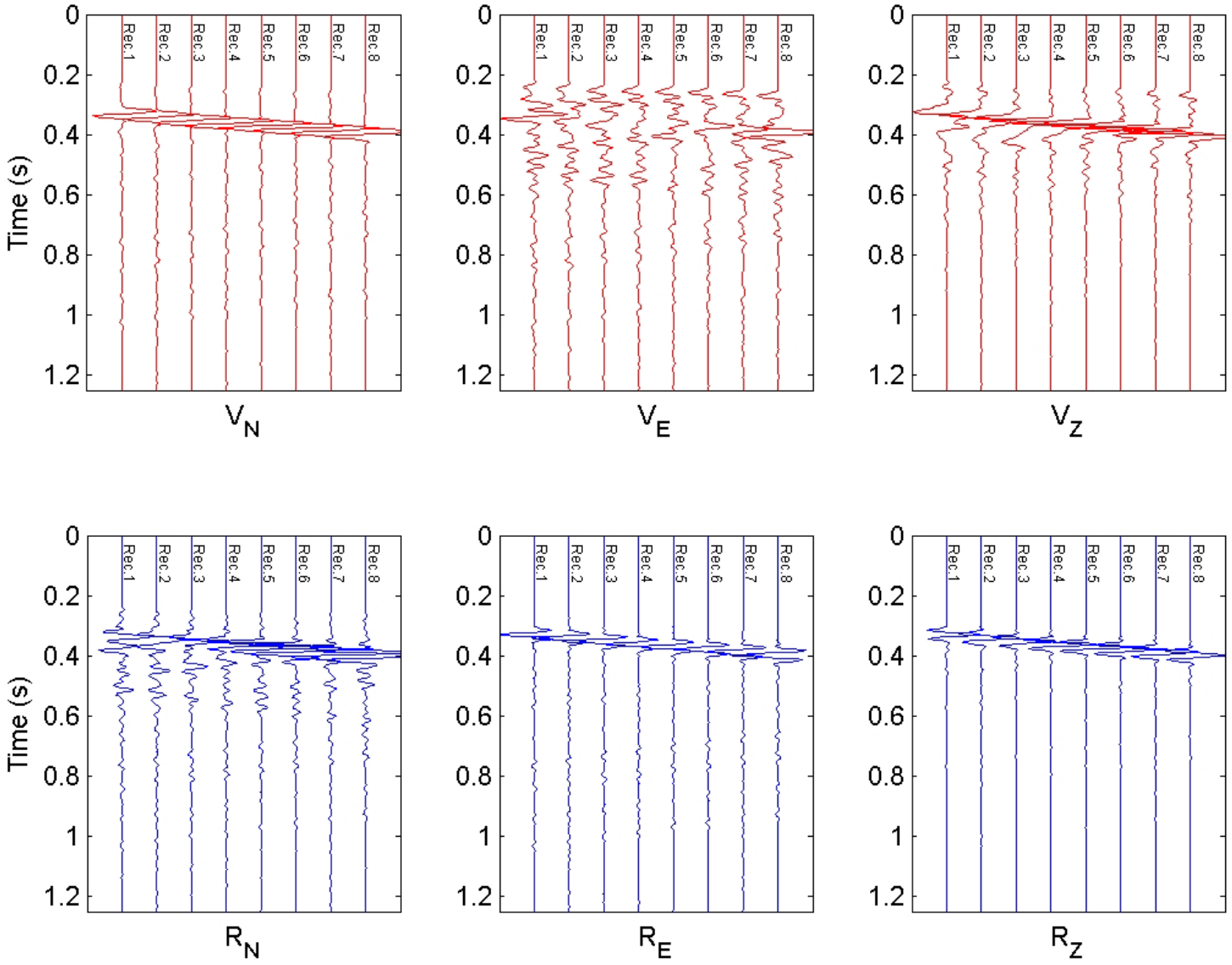

Figure B2. The simulated seismograms for the layered structure with source 5, obtained at the vertical profile (receivers 1 to 8). Top row: translation velocities. Bottom row: rotation rates.

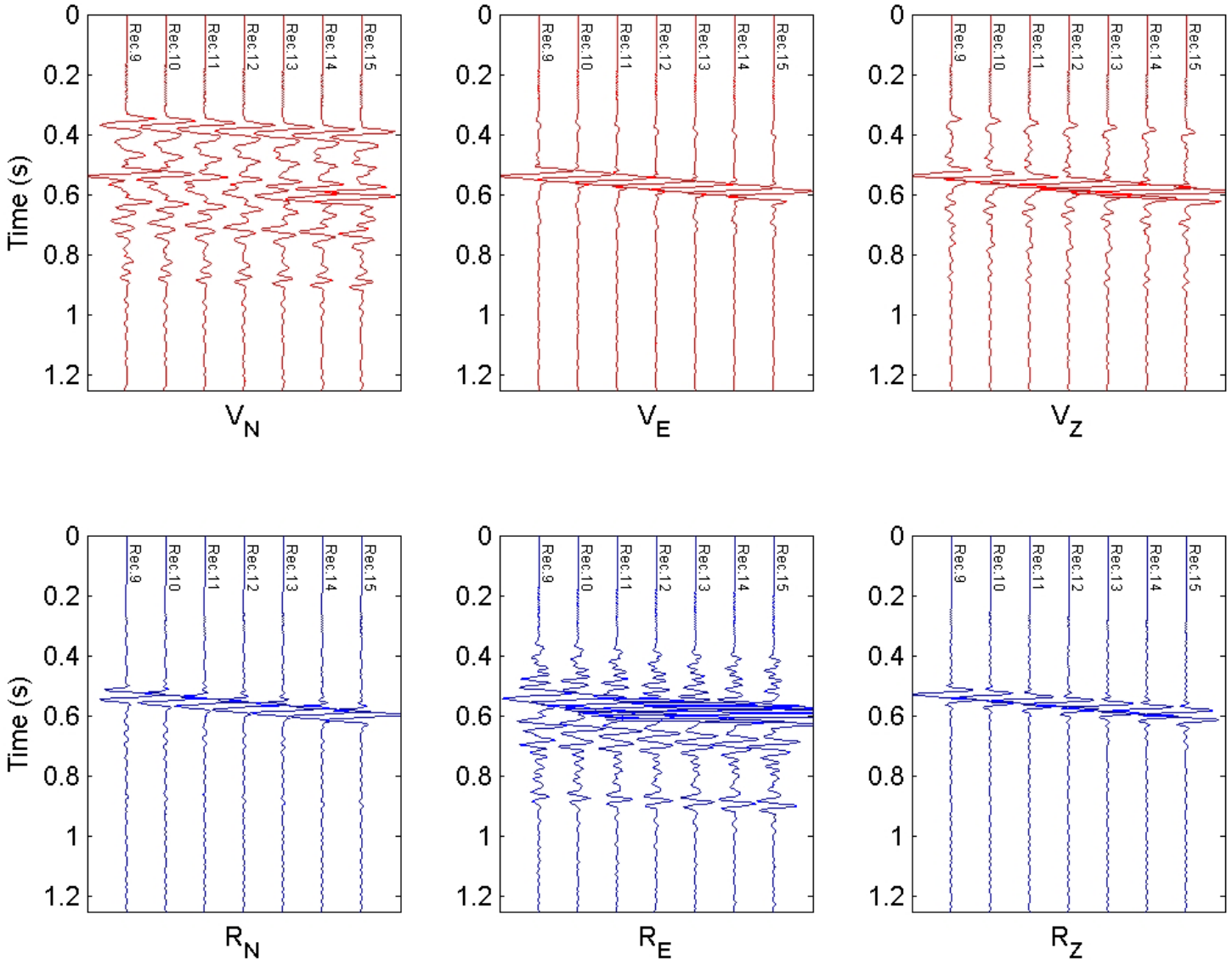

Figure B3. The simulated seismograms for the layered structure with source 5, obtained at the horizontal profile (receivers 9 to 15). Top row: translation velocities. Bottom row: rotation rates.

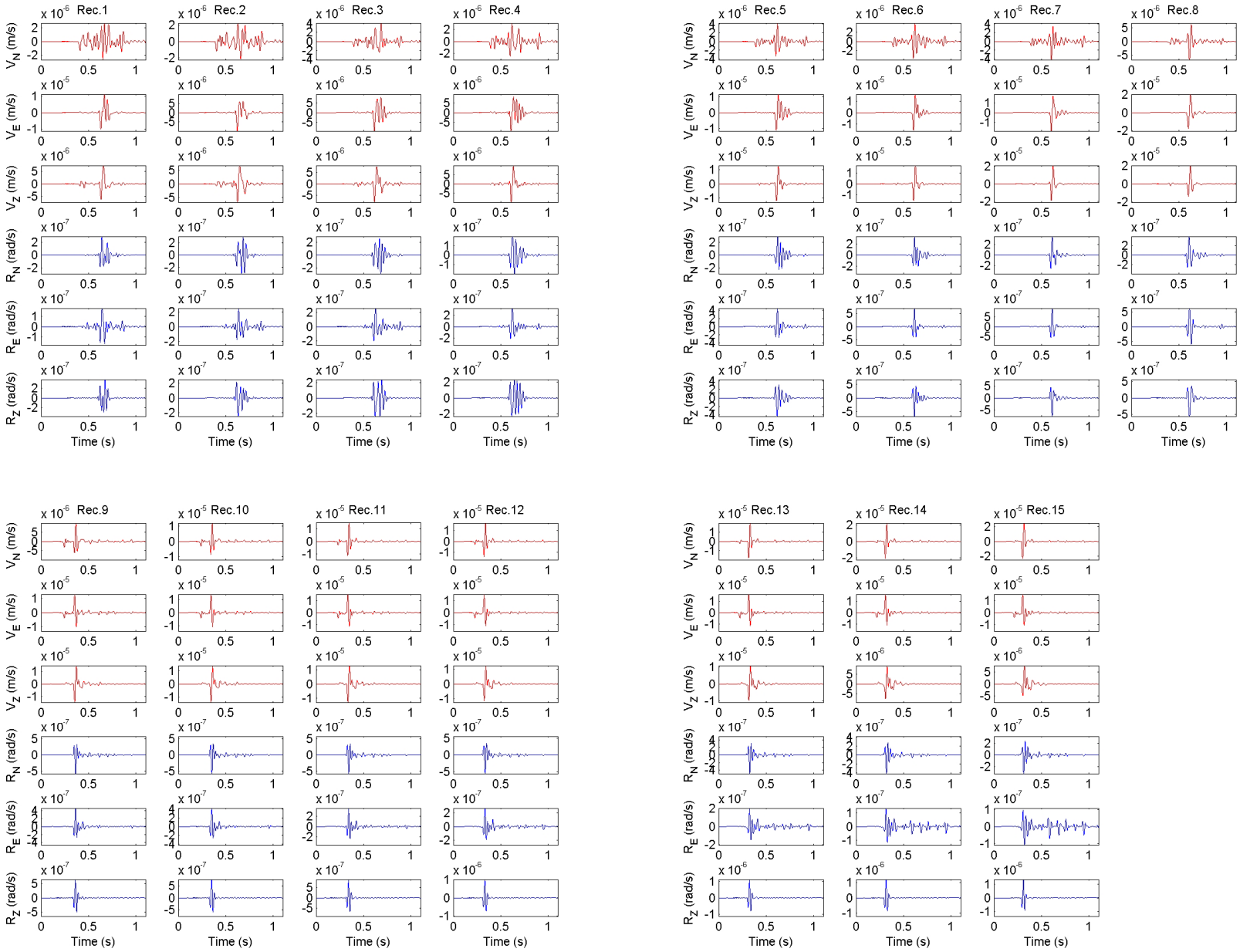

Figure B4. Six component seismograms simulated for the layered structure, source location 1. Red traces: translation velocities; Blue traces: rotation rates.

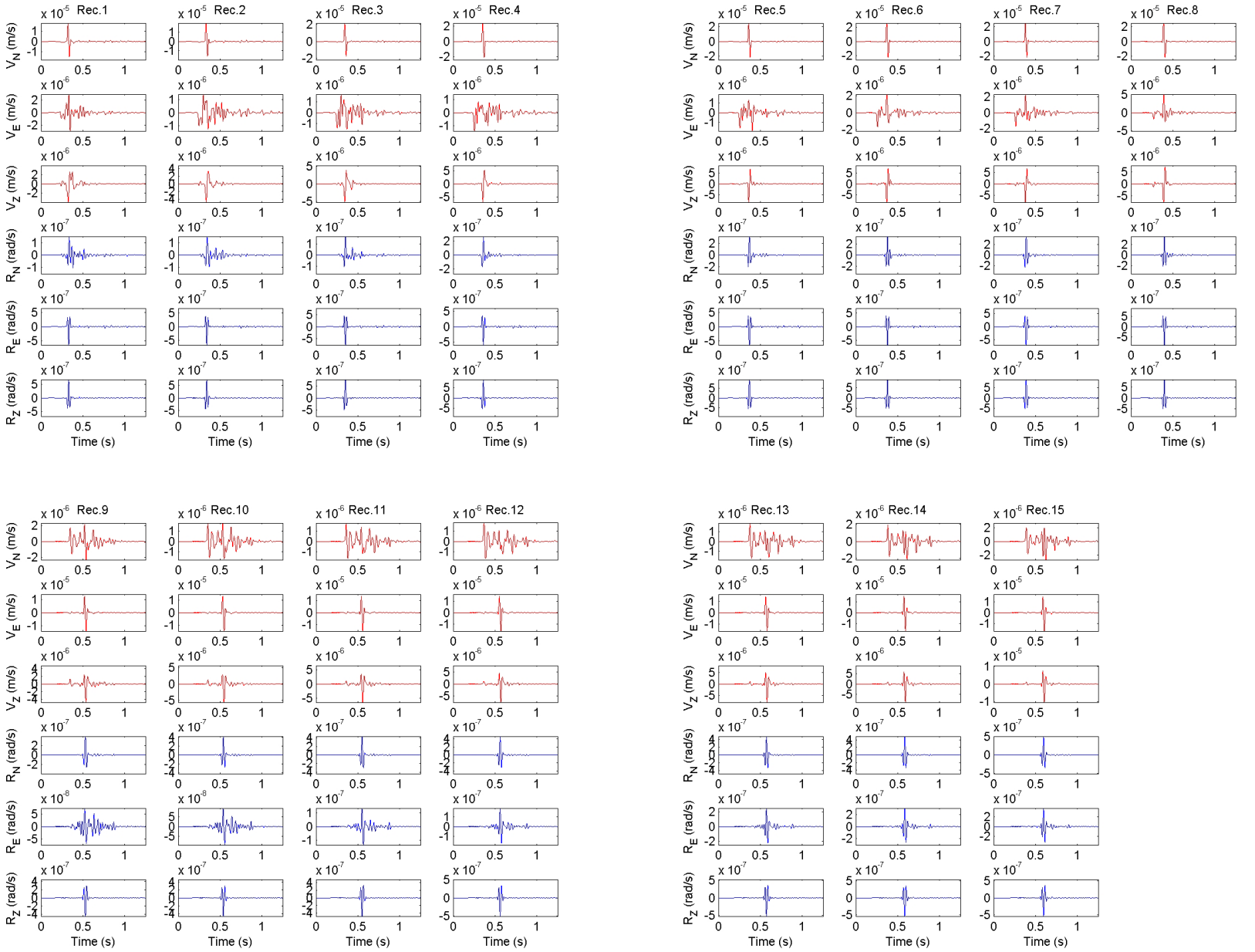

Figure B5. Six component seismograms simulated for the layered structure, source location 5. Red traces: translation velocities; Blue traces: rotation rates.